Insect Biochemistry and Molecular Biology 107 (2019) 19–30

Contents lists available at ScienceDirect

Insect Biochemistry and Molecular Biology

journal homepage: www.elsevier.com/locate/ibmb

Structural and functional characterization of an intradiol ring-cleavage dioxygenase from the polyphagous spider mite herbivore *Tetranychus urticae* Koch

Caleb R. Schlachter[a], Leily Daneshian[a], Jose Amaya[a], Vincent Klapper[a], Nicky Wybouw[b,c], Tomasz Borowski[d], Thomas Van Leeuwen[b,c], Vojislava Grbic[e,f], Miodrag Grbic[e,f], Thomas M. Makris[a], Maksymilian Chruszcz[a,*]

[a] *Department of Chemistry and Biochemistry, University of South Carolina, Columbia, SC, 29208, USA*
[b] *Institute for Biodiversity and Ecosystem Dynamics, University of Amsterdam, Science Park 904, 1098 XH, Amsterdam, the Netherlands*
[c] *Department of Plants and Crops, Ghent University, Ghent, B-9000, Belgium*
[d] *Jerzy Haber Institute of Catalysis and Surface Chemistry, Polish Academy of Sciences, 30–239, Krakow, Poland*
[e] *Department of Biology, Western University, London, Ontario, N6A 5B7, Canada*
[f] *University of La Rioja, Logrono, Spain*

ARTICLE INFO

Keywords:
Two-spotted spider mite
Intradiol ring-cleavage dioxygenase
Horizontal gene transfer
Plant-herbivore interactions
tetur07g02040

ABSTRACT

Genome analyses of the polyphagous spider mite herbivore *Tetranychus urticae* (two-spotted spider mite) revealed the presence of a set of 17 genes that code for secreted proteins belonging to the “intradiol dioxygenase-like” subgroup. Phylogenetic analyses indicate that this novel enzyme family has been acquired by horizontal gene transfer. In order to better understand the role of these proteins in *T. urticae*, we have structurally and functionally characterized one paralog (*tetur07g02040*). It was demonstrated that this protein is indeed an intradiol ring-cleavage dioxygenase, as the enzyme is able to cleave catechol between two hydroxyl-groups using atmospheric dioxygen. The enzyme was characterized functionally and structurally. The active site of the *T. urticae* enzyme contains an Fe^{3+} cofactor that is coordinated by two histidine and two tyrosine residues, an arrangement that is similar to those observed in bacterial homologs. However, the active site is significantly more solvent exposed than in bacterial proteins. Moreover, the mite enzyme is monomeric, while almost all structurally characterized bacterial homologs form oligomeric assemblies. *Tetur07g02040* is not only the first spider mite dioxygenase that has been characterized at the molecular level, but is also the first structurally characterized intradiol ring-cleavage dioxygenase originating from a eukaryote.

1. Introduction

Aromatic compounds are abundantly present within the environment and can have a natural (such as the plant biopolymer lignin) or man-made origin (such as phthalates in papers and several insecticides and cosmetics) (Brown et al., 2004; Guzik et al., 2013d; Sainsbury et al., 2015; Widhalm and Dudareva, 2015). These compounds are extremely stable due to their high resonance energy and are recalcitrant to biodegradation (Brown et al., 2004; Guzik et al., 2013d). The low level of biodegradation leads to an accumulation of aromatic compounds in various animal and plant tissues (Brown et al., 2004). Aromatic compounds serve various biological functions. For instance, many of the plant secondary metabolites that serve in anti-herbivore defense pathways possess an aromatic structure (Widhalm and Dudareva, 2015).

To metabolize aromatic compounds, organisms can be equipped with metalloenzymes termed ring-cleavage dioxygenases that are capable of cleaving aromatic compounds by utilizing a non-heme iron cofactor in the active site (Broderick, 1999; Dermauw et al., 2013). Ring-cleavage dioxygenases belong to two unrelated enzyme families: extradiol and intradiol-ring cleavage dioxygenases (ID-RCDs), where the latter cleave the aromatic ring between two adjacent hydroxyl-groups (Bugg, 2003; Vaillancourt et al., 2006). In contrast to extradiol ring-cleavage dioxygenases that are phylogenetically ubiquitous, intradiol ring-cleavage dioxygenases are largely restricted to bacterial

---

Abbreviations: ID-RCD, intradiol-ring cleavage dioxygenase; MBP, Maltose Binding Protein; ICP-MS, inductively coupled plasma mass spectrometry; LMCT, ligand to metal charge transfer; DSF, Differential Scanning Fluorimetry; β-ME, mercaptoethanol; RMSD, root mean square deviation; PDB, Protein Data Bank

[*] Corresponding author. Department of Chemistry and Biochemistry, University of South Carolina, Columbia, SC 29208, USA.
E-mail address: chruszcz@mailbox.sc.edu (M. Chruszcz).

https://doi.org/10.1016/j.ibmb.2018.12.001
Received 10 October 2018; Received in revised form 20 November 2018; Accepted 4 December 2018

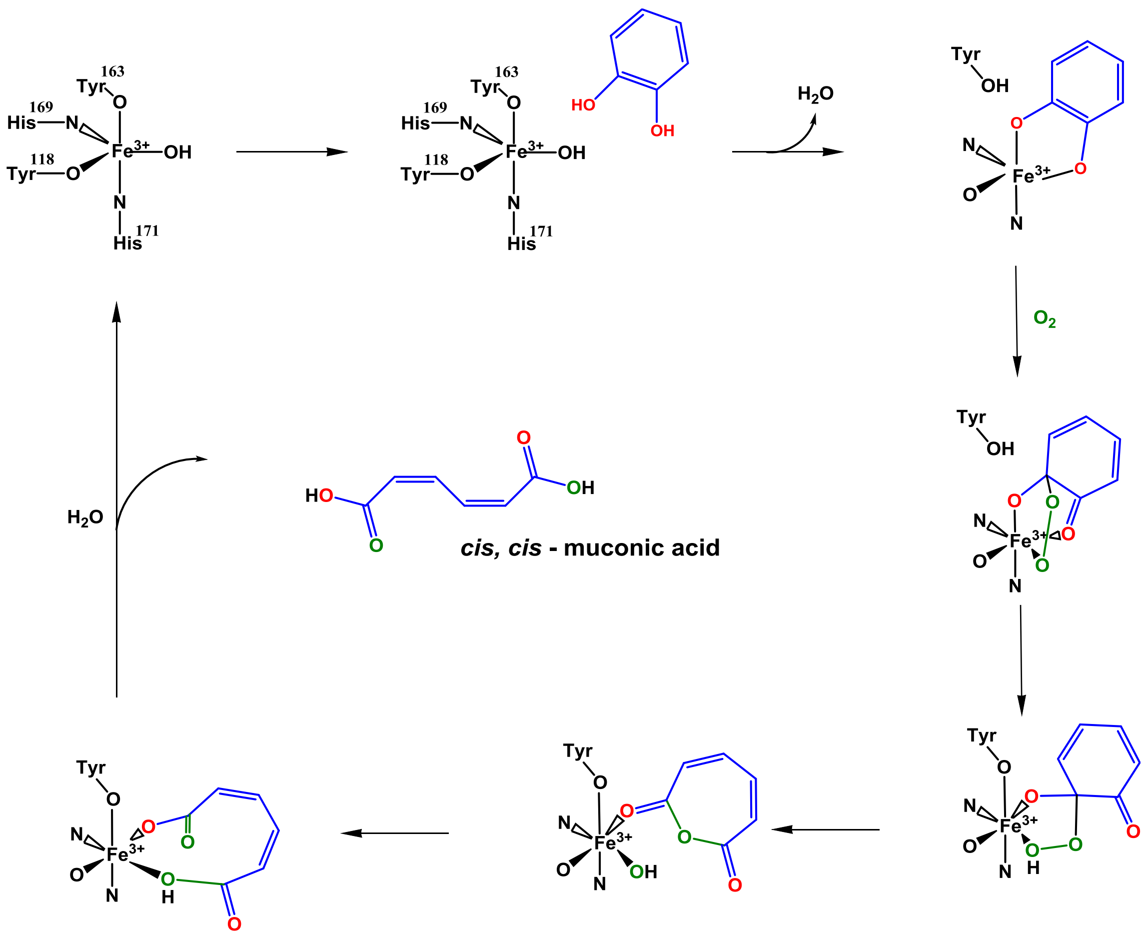

Fig. 1. Schematic diagram of catechol cleavage by an intradiol ring-cleaving dioxygenase (Borowski and Siegbahn, 2006a; Knoot et al., 2015; Wojcik et al., 2011). Residue numbers correspond to those of TuIDRCD.

and fungal species. Genome analyses of the polyphagous spider mite herbivore *Tetranychus urticae* (or the two-spotted spider mite) revealed the presence of a set of 17 genes that code for secreted proteins that belong to the “intradiol dioxygenase-like” subgroup (Dermauw et al., 2013; Grbic et al., 2011). Phylogenetic analyses indicate that this novel enzyme family has been acquired by horizontal gene transfer, a biological process whereby genetic information is asexually transferred between two reproductively isolated and unrelated species. This horizontal acquisition and subsequent proliferation of ID-RCDs may contribute to the polyphagous lifestyle of *T. urticae* by detoxifying allelochemicals produced by its plant hosts (Dermauw et al., 2013). Catechol, or 1,2-dihydroxy benzene, is a common plant metabolite and a substrate for many ID-RCDs (Weng, 2014; Widhalm and Dudareva, 2015). Typically, ID-RCDs detoxify catechols (and catechol derivatives, i.e. substituted with halides, or other functional groups) by cleaving the aromatic ring between C1 and C2, resulting in the formation of *cis, cis*-muconic acid (Fig. 1) that can be further metabolized into succinate and acetyl-CoA (Broderick, 1999; Guzik et al., 2013d).

In order to better understand the role of ID-RCDs in *T. urticae*, we have structurally and functionally characterized *Tetur07g02040*, referred to hereafter as TuIDRCD. TuIDRCD was selected for these studies, as it is the only ID-RCD in *T. urticae* that contains an intron (Dermauw et al., 2013) and is least similar in terms of the protein sequence to other two-spotted spider mite intradiol dioxygenase-like proteins (Supplementary Materials Fig. S1). Here, we have determined the spectroscopic, structural and metabolic properties of TuIDRCD, the first arthropod ID-RCD to be characterized to date. TuIDRCD shows several deviations from the previously crystallized bacterial ID-RCDs, hereby shedding more light on the biological role of ID-RCDs in spider mites and other arthropods.

2. Materials and methods

2.1. Expression and purification of TuIDRCD constructs

The gene coding for *Tetur07g02040* was ordered from ATUM (formerly DNA2.0; Newark, CA), codon optimized for *E. coli* and inserted into pJExpress411 with a T7 promoter, terminator and kanamycin resistance. Initially, the TuIDRCD gene was synthesized with the first 47 amino acids truncated for two reasons: 1) residues 1–22 were predicted to be a signal peptide (Uniprot reference number: T1K8P1) (UniProt, 2015), 2) residues 28–49 were predicted to be disordered (Slabinski et al., 2007). Furthermore, the gene was synthesized to contain an N-terminal cleavable 6xHis-tag for ease of purification with the Tobacco Etch Virus (TEV) protease cut site MHHHHHHSSGVDLGTENLYFQ/SGSG where the cut site is shown with a slash. The protein coded by the initially designed gene is referred as (t48)TuIDRCD in this manuscript (Supplementary Materials, Fig. S2).

Plasmid was transformed into BL-21 (DE3) cells by heat shock and grown in 1.0 L cultures of Luria-Broth (LB) with 50 μg/mL kanamycin or 100 μg/mL ampicillin (depending on construct) shaking at 37 °C until an O.D. of 0.8 was reached. Cultures were cooled to 16 °C and protein expression was induced with 0.4 mM isopropyl β-D-1-thiogalactopyranoside for 16 h while shaking. Cells were pelleted and frozen at −80 °C until needed further.

For purification of (t48)TuIDRCD, cell pellets were resuspended in lysis buffer (50 mM Tris, 500 mM NaCl, 10 mM imidazole, 20 mM β-mercaptoethanol (β-ME), 2% glycerol). After resuspension, cells were lysed by sonication with a Branson 45 Sonifier (ThermoFisher, Grand Island, NY). Crude extract was separated by spinning the lysate in a Beckman Coulter centrifuge (Indianapolis, IN). The clear, yellowish supernatant was poured into a 12 × 1.5 cm Bio-Rad column (Hercules, CA) filled with 5.0 mL of NiNTA resin (ThermoFisher, Grand Island, NY) previously equilibrated in wash buffer (50 mM Tris pH 7.4, 150 mM NaCl, 30 mM imidazole, 2% glycerol, 20 mM β-ME) and then washed with wash buffer. Protein was eluted using elution buffer (50 mM Tris pH 7.4, 150 mM NaCl, 250 mM imidazole, 2% glycerol, 20 mM β-ME) and immediately put into dialysis buffer (50 mM Tris pH 7.4, 150 mM NaCl, 30 mM imidazole) in ThermoFisher SnakeSkin Dialysis Tubing (Grand Island, NY) with a 10,000 MW cutoff. Protein was dialyzed in dialysis buffer for 12 h at 4 °C.

After dialysis, protein was concentrated with Amicon Ultra concentrators (EMD Millipore, Billerica, MA) with a 10,000 MW cutoff. Concentrated protein was put on a Superdex 200 column attached to an ÄKTA Pure FPLC system (GE Healthcare, Marlborough, MA) equilibrated in FPLC buffer (50 mM Tris pH 7.4, 150 mM NaCl, 30 mM imidazole). Peaks corresponding to (t48)TuIDRCD were pooled and the protein concentration was determined using A_{280} with the MW 27,068 Da and molar extinction coefficient 25,900 $M^{-1}cm^{-1}$ as determined by using ExPASy ProtParam tool (Gasteiger et al., 2003).

Purified (t48)TuIDRCD was red in color, indicating the presence of non-heme ferric iron, but the protein was very unstable and frequent red precipitate was observed in purified protein samples. Due to instability, constructs with the fusion partner Maltose-Binding Protein (MBP) were pursued where all purification buffers had the addition of 5.0 mM maltose. In addition, a construct including residues 23–259, TuIDRCD, was also expressed and purified which showed greater stability than (t48)TuIDRCD.

The (t48)TuIDRCD-MBP yielded decent amounts of protein (~10 mg/L culture); however, the protein did not have the red hue observed from (t48)TuIDRCD purification that was indicative of non-heme iron (and most likely properly folded protein) so this construct was not pursued further. MBP-(t48)TuIDRCD and mTuIDRCD yielded decent quantities of protein (~8 mg/L culture) and had the desired red hue after purification. Protein yields were increased by adding 3.0 mg of ferrous sulfate heptahydrate to the 1.0 L LB culture pre-induction and to the lysis buffer. Protein concentration was determined using A_{280} with the MW 67,027 Da and 27,063 Da, and molar extinction coefficients 92,375 $M^{-1}cm^{-1}$ and 24,410 $M^{-1}cm^{-1}$, for MBP-(t48)TuIDRCD, and mTuIDRCD, respectively. Attempts were not made to remove the His-tag from MBP-dioxygenase due to the presence of a potential TEV cut site in the MBP sequence. The His-tag was cleaved from mTuIDRCD with TEV protease after a 16 h incubation at 4 °C in dialysis buffer; mTuIDRCD was collected by flowing the solution over an NiNTA column equilibrated in dialysis buffer.

2.2. Molecular cloning of TuIDRCD into pMCSG29

The dioxygenase gene coding for residues 48–259 was cloned into pMCSG29 (Eschenfeldt et al., 2013) using ligation independent cloning (LIC). This plasmid is designed to generate a fusion protein as follows: protein of interest, TEV protease cut site, 6xHis-tag, Tobacco Vein Mottling Virus (TVMV) protease cut site, MBP). The protein coded by this construct is referred to as (t48)TuIDRCD-MBP (Fig. S3). For details of the cloning protocols see Supplementary Materials).

Clones were miniprepped with a GeneJET Plasmid Miniprep Kit (ThermoFisher, Grand Island, NY) and insertion of ID-RCD was first confirmed by restriction digest with XhoI following the manufacturer's instructions (NEB, Ipswich, MA). After restriction digest, clones with correctly sized fragments were sent to EtonBioscience (Research Triangle Park, NC) for sequencing with T7 forward and T7 reverse primers.

2.3. Cloning TuIDRCD into pMBPcs1

The pMBPcs1 plasmid was generated and amplified as previously described (Schlachter et al., 2017). The (t48)TuIDRCD gene was cloned into pMBPcs1 using LIC, and this construct is referred to as MBP-(t48)TuIDRCD (Fig. S4).

Clones were miniprepped with a GeneJET Plasmid Miniprep Kit (ThermoFisher, Grand Island, NY) and insertion of dioxygenase was first confirmed by restriction digest with HindIII and XbaI following the manufacturer's instructions (NEB, Ipswich, MA). After restriction digest, clones with correctly sized fragments were sent to EtonBioscience (Research Triangle Park, NC) for sequencing with T7 forward and T7 reverse primers.

2.4. Generation of mature TuIDRCD (mTuIDRCD)

Originally, the first construct for TuIDRCD was ordered from ATUM (Newark, CA) as a truncated protein with the first 47 amino acids missing. To observe if the predicted, unstructured residues have an impact on protein stability, residues 23–47 (25 residues total) were cloned into the (t48)TuIDRCD construct to produce mature TuIDRCD (residues 23–259, mTuIDRCD, Fig. S5)).

Primers Dioxy25-F and Dioxy25-R in Table S2 were used to produce a fragment containing the desired 25 amino acids. The fragment was generated and amplified by using PCR with Q5 polymerase (NEB, Ipswich, MA) following the manufacturer's protocol. To insert the fragment into the TuIDRCD construct, primers p411-Dioxy25-F and p411-Dioxy25-R were used to generate megaprimers of the fragment.

Clones were selected, miniprepped, and insertion of the fragment was confirmed by sending plasmids for sequencing to EtonBioscience (Research Triangle Park, NC) using T7 forward and T7 reverse primers.

2.5. Differential Scanning Fluorimetry

Differential Scanning Fluorimetry was performed as described previously (Booth et al., 2018). Briefly, fluorescence data was collected by a Bio-Rad CFX96 RT-PCR instrument (Hercules, CA). SYPRO® Orange Dye (ThermoFisher, Waltham, MA) was diluted 1:1000 in 1.0 mL of 1 mg/mL protein (mTuIDRCD with cleaved his-tag). The solution of the dye and protein was mixed with each pH and salt screen condition 1:1 for a 20 μL total reaction volume. Bio-Rad Hardshell 96-well RT-PCR plate was used and sealed with Bio-Rad Microseal PCR Plate Sealing Film (Hercules, CA). Emission was measured at 590 nm (excitation at 488 nm) at temperatures increasing in the range of 30–90 °C with a 1 °C/min in 2 °C increments. All screen conditions had working concentrations of 50 mM buffer with a pH range of 4–9.5 in 0.5 pH unit increments and a sodium chloride range from 0 to 1.0 M (No salt, 0.05 M, 0.10 M, 0.15 M, 0.20 M, 0.25 M, 0.50 M and 1.0 M). Buffers used to maintain the pH ranges were acetate (pH 4.0–5.0), Bis-Tris (pH 5.5–6.5), Tris (pH 7.0–8.0) and CHES (pH 8.5–9.5). Each experiment was performed in triplicate.

2.6. Activity assay

All reagents for enzymatic assays were purchased from Sigma-Aldrich (St. Louis, MO). Assays were performed using catechol (1,2-dihydroxybenzene) and 4-methylcatechol as substrate following the protocol described previously (Guzik et al., 2013d). Cleavage of substrate was monitored by measuring the A_{260} nm and A_{255} nm of the product *cis,cis*-muconic acid and 3-methylmuconic acid with a molar extinction coefficient of 16,800 $M^{-1}cm^{-1}$ and 14,300 $M^{-1}cm^{-1}$ respectively. The measurements were performed with Synergy H1 Hybrid Multi-Mode Microplate Reader (Biotek, Winooski, VT). The production of *cis,cis*-muconic acid was confirmed using liquid chromatography mass spectrometry and NMR (data not shown). Reactions were performed using 200 μL total with working concentrations of 100 mM

Table 1

Summary of kinetic data (25 °C) for cleavage of catechol and 4-methylcatechol by the His-tag cleaved version of mTuIDRCD.

Buffers	pH	K_M (μM)	V_{max} (μMmin^{-1})	k_{cat} (min^{-1})	k_{cat}/K_M (μM^{-1}min^{-1})
Catechol					
Sodium phosphate	6.0	9.90 ± 0.97	0.128 ± 0.002	0.025 ± 0.001	0.002 ± 0.001
Sodium phosphate	6.5	11.8 ± 1.3	0.231 ± 0.005	0.046 ± 0.001	0.003 ± 0.001
Sodium phosphate	7.0	14.5 ± 1.9	0.32 ± 0.01	0.064 ± 0.002	0.004 ± 0.001
Sodium phosphate	7.5	16.9 ± 1.7	0.52 ± 0.01	0.104 ± 0.002	0.006 ± 0.001
HEPES	8.0	23.9 ± 2.7	1.02 ± 0.03	0.204 ± 0.006	0.008 ± 0.002
AMPSO	8.5	26.2 ± 2.6	1.14 ± 0.03	0.228 ± 0.006	0.008 ± 0.002
AMPSO	9.0	30.2 ± 3.7	1.25 ± 0.04	0.250 ± 0.008	0.008 ± 0.002
AMPSO	9.5	40.8 ± 6.3	1.37 ± 0.07	0.274 ± 0.014	0.006 ± 0.002
4-Methylcatechol					
Sodium phosphate	6.0	13.3 ± 1.2	0.201 ± 0.004	0.402 ± 0.008	0.030 ± 0.001
Sodium phosphate	6.5	21.1 ± 3.5	0.22 ± 0.01	0.44 ± 0.02	0.020 ± 0.001
Sodium phosphate	7.0	25.7 ± 5.2	0.53 ± 0.02	1.06 ± 0.04	0.040 ± 0.001
Sodium phosphate	7.5	29.3 ± 3.5	0.59 ± 0.02	1.18 ± 0.04	0.04 ± 0.01
HEPES	8.0	48.3 ± 5.5	1.35 ± 0.05	2.70 ± 0.10	0.05 ± 0.01
AMPSO	8.5	56.0 ± 7.7	1.41 ± 0.07	2.82 ± 0.14	0.05 ± 0.01
CHES	9.0	99.8 ± 13.2	1.90 ± 0.10	3.80 ± 0.20	0.03 ± 0.01
CHES	9.5	123.6 ± 10.5	2.23 ± 0.08	4.46 ± 0.16	0.03 ± 0.01

sodium phosphate (pH 6.0), Bis-Tris (pH 6.5), Tris-HCl (pH 7.0, 7.5, and 8.0), AMPSO or AMPSO/CHES (pH 8.5, 9.0, and 9.5), 5 μM (for catechol) or 0.5 μM (for 4-methylcatechol) protein (mTuIDRCD with cleaved his-tag), and 1–200 μM substrate. Activity was measured for 20 min. All measurements were performed in triplicate and data were fit by Origin software (Matera et al., 2010) and Microsoft Excel using the Solver add-on. Experimental results are summarized in Table 1.

2.7. Ferrozine assay

Ferrozine assay was used to check whether the purified recombinant protein contains iron (Tchesnokov et al., 2012). All reagents for the ferrozine assay were purchased from Sigma-Aldrich (St. Louis, MO). Initially, 30 μM protein was incubated and hydrolyzed by 0.5 M HCl overnight at room temperature. Next, reducing reagent was added to the mixture and incubated for 30 min at room temperature for a final concentration of 0.2 M hydroxylamine (1.4 M hydroxylamine stock was prepared using 2 M HCl). Lastly, working concentrations of 0.8 mM ferrozine (10 mM ferrozine stock was prepared using 100 mM ammonium acetate) and 0.6 M ammonium acetate buffer (5 M buffer stock was prepared using ammonium hydroxide (pH 9.5)) were added and the absorbance was measured at 562 nm with the molar extinction coefficient of 27,900 M^{-1}cm^{-1} on a Hewlett-Packard 8453 spectrophotometer (Palo Alto, CA). The standard curve was prepared using iron (III) chloride in the range of 5 μM–60 μM following the same procedure.

2.8. Inductively coupled plasma mass spectrometry (ICP-MS)

For further investigation of the iron content ICP-MS was performed (Becker et al., 2010). Briefly, 200 μg of protein was prepared in 2% nitric acid and filtered by 0.2-μm (Whatman Nylon Puradisc) syringe filter. Finnigan ELEMENT XR double focusing magnetic sector field inductively coupled plasma-mass spectrometer (SF-ICP-MS) was used for the analysis with Ir and/or Rh as internal standards. 0.2 mL/min Micromist U-series nebulizer (GE, Australia), quartz torch and injector (Thermo Fisher Scientific, USA) were used for sample introduction. Sample gas flow was at 1.08 mL/min.

2.9. UV-VIS spectroscopy

To assess whether the available iron is bound to the protein, the whole spectrum was measured. Protein concentration was measured at 280 nm on Cary 50 UV–Vis Spectrophotometer (Agilent, Santa Clara, CA) with molar extinction coefficients determined by ExPASy ProtParam. Next, the absorbance at 430 nm was determined and the molar extinction coefficient for the tyrosine to iron charge transfer transmission was calculated.

2.10. Crystallization of MBP-(t48)TuIDRCD and mTuIDRCD

All chemicals were purchased from Hampton Research (Aliso Viejo, CA), ThermoFisher (Grand Island, NY) or Sigma-Aldrich (St. Louis, MO). Crystallization experiments were performed at room temperature using the sitting-drop vapor diffusion method and MRC 2-drop 96-well crystallization plates (Hampton Research, Aliso Viejo, CA). Initially, MBP-(t48)TuIDRCD crystals were grown in 0.1 M sodium cacodylate trihydrate pH 6.5, 0.2 M magnesium acetate tetrahydrate, 20% w/v PEG8000 (3:1 of protein:mother liquor where protein ∼13 mg/mL). These red colored crystals were microseeded due to their small size. For microseeding, crystals were crushed and resuspended in a 1.5 mL tube filled with 150 μL of the cacodylate crystallization solution and a glass bead then vortexed. An equal volume of MBP-(t48)TuIDRCD (∼13 mg/mL) was added to the seed stock and drops were set with 1:1 ratio of protein to mother liquor as written above. Using the seed stock, red crystals grew after about one month in 0.1 M Tris pH 7.5, 15% w/v PEG6000. The mTuIDRCD crystals were obtained using vapor diffusion and sitting drop setup. Drops were formed by mixing protein (1.1 mg/mL) and mother liquor 1:1. The mother liquor contained 0.2 M Li_2SO_4, 0.1 M HEPES pH 7.5, 10% w/v PEG3350 and 10 mM catechol. All crystallization experiments were performed at 25 °C.

2.11. Data collection, structure determination and refinement

Table 2 shows the data collections statistics for crystal structures of mbp-(t48)TuIDRCD (residues 48–259; truncation product of MBP-(t48)TuIDRCD) and mTuIDRCD (residues 23–259). The crystal structures for mbp-(t48)TuIDRCD and mTuIDRCD were deposited in the Protein Data Bank (PDB) (Berman et al., 2000) with the accession codes 5VG2 and 6BDJ. Crystals were cryo-cooled in liquid nitrogen and data was collected using the Southeast Regional Collaborative Access Team (SER-CAT) 22ID beamline at the Advanced Photon Source (APS), Argonne National Lab (Argonne, IL). Data were processed with the HKL-2000 software package (Otwinowski and Minor, 1997). Molecular replacement for mbp-(t48)TuIDRCD was performed using MOLREP (Vagin and Teplyakov, 1997) integrated with HKL-3000 (Minor et al., 2006) and the PDB entry 4ILT as a starting model. BUCCANEER (Cowtan, 2006) and HKL-3000 were used to rebuild the initial model. Refinement was performed using REFMAC (Murshudov et al., 2011) and HKL-3000. Non-crystallographic symmetry was used during the

Table 2
Data collection and refinement statistics for TuIDRCD. Values in parentheses are for the highest resolution shell.

Protein	mbp-(t48)TuIDRCD	mTuIDRCD
PDB accession code	5VG2	6BDJ
Data Collection		
Diffraction source	APS, 22ID	APS, 22ID
Wavelength (Å)	1.000	1.000
Space group	P2	P2
a, *b*, *c*, *β* (Å, °)	60.5, 43.1, 165.7, 95.2	61.1, 45.4, 83.0, 94.3
Resolution range (Å)	50.0–2.45 (2.49–2.45)	40.0–2.15 (2.19–2.15)
No. of unique reflections	30081 (1539)	24133 (929)
Completeness (%)	95.5 (97.7)	95.3 (72.3)
Redundancy	3.1 (3.0)	4.0 (3.1)
$\langle I/\sigma(I)\rangle$	14.5 (2.0)	32.0 (3.4)
$R_{\text{r.i.m.}}$	0.116 (0.665)	0.064 (0.300)
$R_{\text{p.i.m.}}$	0.064 (0.371)	0.032 (0.160)
Overall B factor from Wilson plot (Å^2)	37.3	49.8
Refinement		
Resolution range (Å)	50.0–2.45 (2.52–2.45)	40.0–2.15 (2.21–2.15)
Completeness (%)	95.0 (90.2)	95.3 (76.2)
No. of reflections, working set	28666 (2007)	22883 (1321)
No. of reflections, test set	1414 (103)	1095 (62)
Final R_{cryst}	0.191 (0.271)	0.214 (0.266)
Final R_{free}	0.231 (0.284)	0.248 (0.286)
Rmsd Bonds (Å)	0.015	0.011
Rmsd Angles (°)	1.7	1.6
Ramachandran Plot		
Most favored (%)	97	97
Allowed (%)	100	100

whole process of refinement. TLS refinement was used during the last stages of refinement and the TLS Motion Determination server was used for partitioning protein chains into the rigid bodies undergoing vibrational motions (Painter and Merritt, 2006). Model was updated and validated with COOT (Emsley and Cowtan, 2004). MOLPROBITY was used in the final steps of the model validation (Davis et al., 2007). A similar approach was used for determination, refinement, and validation of mTuIDRCD structure; however, in this case the structure of mbp-(t48)TuIDRCD (PDB code: 5VG2) was used as the starting model for molecular replacement.

2.12. EPR spectra

EPR spectra of the as-isolated enzyme were recorded using an X-band Bruker EMXplus spectrometer (Bruker Bio Spin, Billerica, MA) equipped with an Oxford Instruments ESR900 (Oxfordshire, UK) liquid helium continuous flow cryostat. Spectra were recorded at a temperature of 12 K and a 1 mT modulation amplitude. MBP-(t48)TuIDRCD and mTuIDRCD protein concentrations were 120 and 200 μM, respectively. The nitrosyl complexes were prepared in a Coy anaerobic chamber after degassing the protein with N_2. The enzyme was treated with 3 molar equivalents of methyl viologen, 9 molar equivalents of sodium dithionite and 1 molar equivalent of MAHMA NONOate (2 molar equivalents of NO per protein) prior to flash freezing in liquid nitrogen.

2.13. Various computational calculations

XtalPred was used to design the original construct for TuIDRCD (Slabinski et al., 2007). The programs ProFunc and PDBePISA were used to analyze the crystal structures (Krissinel and Henrick, 2007; Laskowski, 2017). COOT, PyMOL (DeLano W., 2002) and UCSF-Chimera (Pettersen et al., 2004) were used to visualize and analyze the structures, as well as to generate figures. APBS (Jurrus et al., 2018) as implemented in PyMOL was used for electrostatics calculations. DALI (Holm and Rosenstrom, 2010) and PDBeFold (Krissinel and Henrick, 2004) were used to search for similar structures. The pI values were calculated using ExPASy ProtParam tool.

2.14. Phylogenetic analysis

Based on previous studies, the closest homologs to *tetur07g02040* within Tetranychidae were included in the phylogenetic analysis (Bajda et al., 2015; Dermauw et al., 2013). In addition, arthropod and tardigrade genome assemblies were mined for the presence of ID-RCD genes via local tBLASTn-searches using *tetur07g02040* as a query. Contamination of genome assemblies was examined by identifying neighboring eukaryotic genes on scaffolds/contigs and by verifying a continuous Illumina- and PacBio-read coverage across the coding region in case of the collembolan genome assemblies (*Folsomia candida* and *Orchesella cincta*) (http://www.collembolomics.nl/). Alignments and Conserved Domain-searches showed that an ID-RCD gene appeared to be incorrectly annotated within the *B. tabaci* genome portal (Chen et al., 2016) and we included the NCBI annotation in our phylogenetic dataset (Supplementary Table S3). The final set of 67 protein sequences were aligned using MAFFT (G-INS-I settings). The protein model of WAG + I + G + F was selected based on the Akaike Information Criterion using ProtTest 3.4.4 (Darriba et al., 2011). A phylogenetic tree was constructed based on Bayesian inference using Mr Bayes v3.2.6 (Ronquist et al., 2012). With seed and nswaps set at 21343 and 3, respectively, 7 heated chains were implemented in the MCMC analysis and were sampled every 100 generations. A total of 1,100,000 generations were run, which resulted in a final average standard deviation of split frequencies of 0.0128.

3. Results

3.1. Phylogenetic analysis

Arthropod genome mining revealed the presence of an ID-RCD gene embedded within the *Bemisia tabaci* genome (Hexapoda: Hemiptera), an apparent horizontal gene transfer event that was not previously detected (Chen et al., 2016). Mites within the Sarcoptiformes lineage (Chelicerata: Acariformes) also possessed ID-RCD genes within their genomes (Fig. 2). Finally, our genome screens also confirmed the presence of ID-RCD genes in collembolan genomes (Hexapoda: Entomobryomorpha) and in genomes of species that belong to the Tardigrada phylum (Faddeeva-Vakhrusheva et al., 2016; Yoshida et al., 2017). The Bayesian inference-based phylogenetic reconstruction indicated that the *B. tabaci* and tardigrade dioxygenase genes have a bacterial and fungal origin, respectively, and reflect independent horizontal gene transfer events (Fig. 2). In contrast, the precise evolutionary origin and history of the dioxygenases of the collembolan and sarcoptiform mite lineages remain unclear, but our phylogenetic reconstruction tentatively suggested a common fungal origin. The monophyletic clade that holds TuIDRCD and close spider mite homologs supported the previously postulated evolutionary scenario wherein a single horizontal gene transfer event from a fungal donor species occurred prior to speciation within the tetranychid spider mite family (Fig. 2) (Bajda et al., 2015; Dermauw et al., 2013).

3.2. TuIDRCD constructs – protein production

In total, four TuIDRCD constructs were produced (see Materials and methods, and Supplementary Figs. S2–S5) due to initial solubility issues of the protein. Two of these constructs ((t48)TuIDRCD and mTuIDRCD) contained a hexahistidine tag and residues corresponding to the spider mite protein, while two additional constructs ((t48)TuIDRCD-MBP and MBP-(t48)TuIDRCD) were fused to Maltose Binding Protein (MBP). The (t48)TuIDRCD construct, where (t48) indicates truncation of the first 47 residues, was generated because this region was initially predicted to be

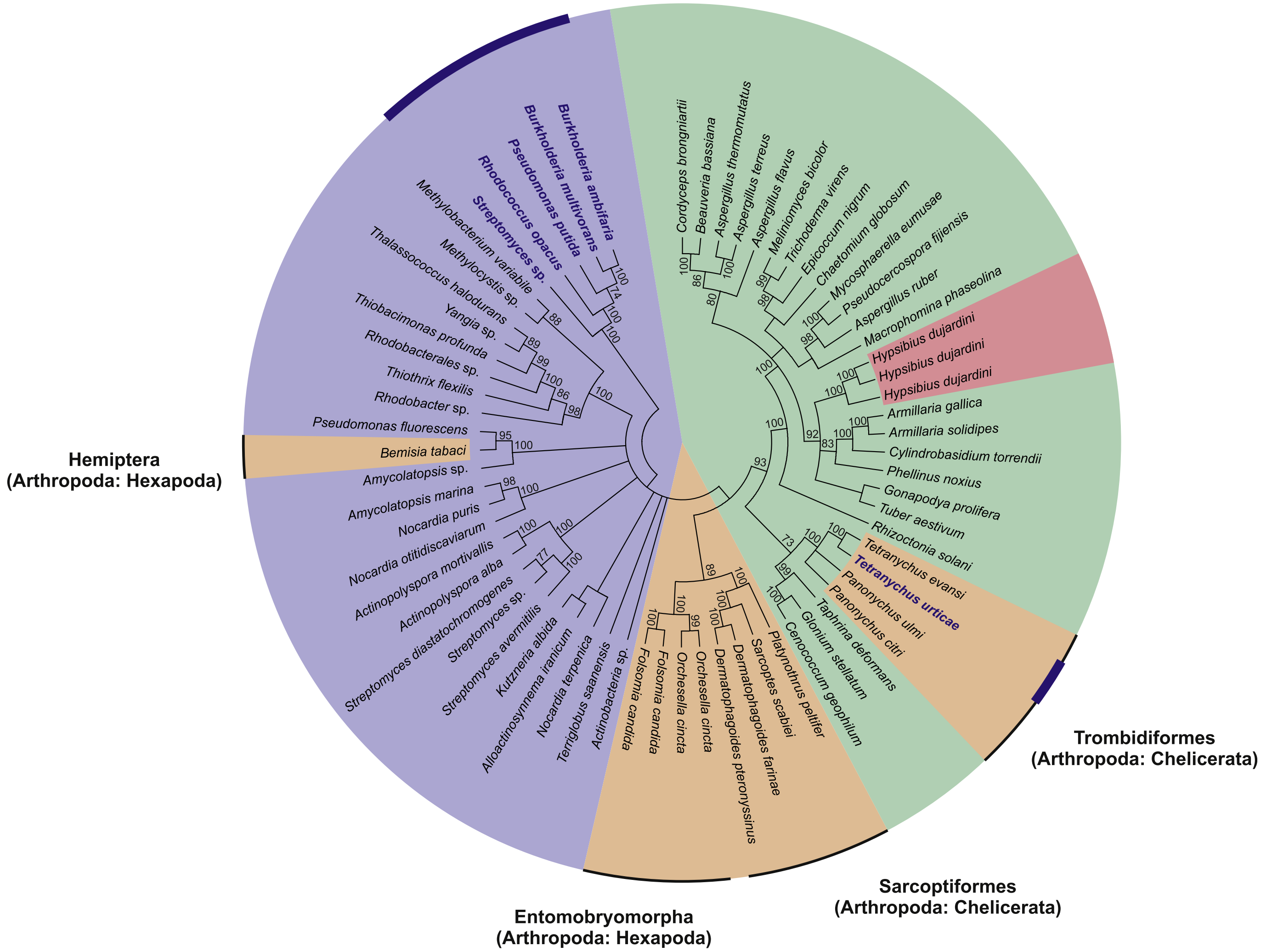

Fig. 2. Phylogenetic reconstruction of the evolutionary history and origin of tardigrade and arthropod intradiol ring-cleavage dioxygenases using a Bayesian method. Only Bayesian posterior probabilities higher than 75 are depicted. Enzymes of which the crystal structure has been determined are indicated by a blue bold font and a blue circumferential line. The colored background reflects the position of the species within the tree of life with bacteria: blue, fungi: green, arthropods: orange and tardigrades: red. The distinct taxa within the Arthropoda phylum are delineated with a black circumferential line, detailing the respective orders and subphyla. (For interpretation of the references to color in this figure legend, the reader is referred to the Web version of this article.)

disordered based on results from XtalPred (Slabinski et al., 2007). However, the protein was found to be unstable. Likewise, (t48)TuIDRCD-MBP, where MBP is fused to the C-terminal end, was colorless which is consistent with the absence of Fe^{3+} in the active site. Two additional constructs, MBP-(t48)TuIDRCD (MBP fused to N-terminal) and mTuIDRCD, were found to contain a pink hue and to contain iron, and were thus selected for the structural and spectroscopic studies described below. The latter mTuIDRCD construct, is comprised of residues 23–259 that correspond to a mature form of the enzyme and was used for activity studies.

3.3. UV–visible and electron paramagnetic resonance spectroscopy

As the presence of the Fe^{3+} cofactor is critical for ID-RCD activity, the iron content of mTuIDRCD was first confirmed using metal-counting procedures that included the ferrozine assay (Tchesnokov et al., 2012) and inductively coupled plasma mass spectrometry (ICP-MS). Together, the results indicated that the purified protein contained 0.98 nmol Fe per nmol protein. ICP also revealed the presence of a minor manganese contaminant (0.11 nmol per nmol protein, Table S1) and no other metal was present in significant abundance. The presence of the iron cofactor was further probed by optical spectroscopy. The optical spectroscopic features were similar for both MBP-(t48)TuIDRCD and mTuIDRCD. The optical spectra of mTuIDRCD and MBP-(t48)TuIDRCD are shown in Fig. 3A and Fig. S6A respectively. Both constructs exhibited absorption features at 325 and 460 nm. The latter feature, with an extinction coefficient ε_{460} $\sim 2500\,M^{-1}cm^{-1}$, is attributed to a mixture of several ligand to metal charge transfer (LMCT) transitions from the axial and equatorial tyrosinate ligands to Fe^{3+}, giving rise to its characteristic burgundy color (Davis et al., 2002). EPR spectroscopy was used to further probe the oxidation state and ligand environment of the iron cofactor. The EPR spectra of both constructs were similar and shown in Fig. 3B (mTuIDRCD) and Fig. S6B (MBP-(t48)TuIDRCD) respectively. Both constructs exhibit two main resonances at $g = 9.25$ and 4.29, which is diagnostic for a high-spin ferric center and nearly identical to those observed for other intradiol dioxygenases such as the well-characterized protocatechuate 3,4-dioxygenase from *Brevibacterium fuscum* (Orville and Lipscomb, 1993). No evidence for Mn^{2+} was observed. In order to further verify the presence of bound Fe^{3+}, the nitrosyl complex of MBP-(t48)TuIDRCD was prepared through reduction of the enzyme with dithionite followed by exposure to NO (Fig. S7). The resulting EPR spectrum exhibits is readily differentiated from the resting state of the enzyme, and is consistent with assignment as an $S = 3/2$ complex that arises from

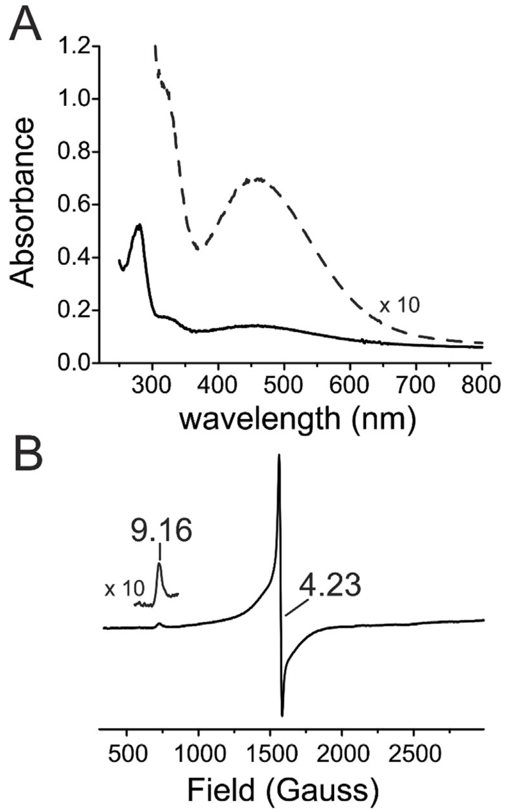

Fig. 3. UV–visible (A) and electron paramagnetic resonance (B) spectra of as-purified mTuIDRCD.

antiferromagnetic coupling between the oxidized iron and bound diatomic ligand.

3.4. mTuIDRC stability and enzymatic activity

The mTuIDRC was found to be relatively stable across a broad pH range and salt concentrations (Fig. 4A) as determined with Differential Scanning Fluorimetry (DSF). The highest thermal stability of the mTuIDRCD was observed in basic solutions.

The kinetic parameters of mTuIDRCD have been determined for catechol at different pH values (Table 1). The k_{cat} increases slightly at basic pH values. The k_{cat} and catalytic efficiency are approximately 10-fold and 4-fold higher, respectively, at pH 8–9 compared to pH 6 (Fig. 4B). The K_M for catechol is similar to those observed for previously characterized enzymes; however, the k_{cat} and catalytic efficiency are significantly lower (as much as 4 orders of magnitude) than those reported for bacterial homologs (Caglio et al., 2009; Ferraroni et al., 2006, 2013; Guzik et al., 2013a; Knoot et al., 2015; Matera et al., 2010; Travkin et al., 1997). Based on thermal stability studies with DSF (Fig. 4A), mTuIDRCD is significantly more stable at basic pH which correlates with enzymatic activity. Increased enzymatic activity at basic pH has been observed for other ID-RCDs (Caglio et al., 2013; Guzik et al., 2013b; Tsai and Li, 2007). Activity of mTuIDRCD was also tested on 3,4-dihydroxybenzoate (protocatechuate), but no activity was observed. On the other hand, 4-methylcatechol was readily cleaved by mTuIDRD with significantly better efficiency (> 10 fold higher k_{cat}) than catechol (Table 1).

3.5. Crystal structures of mbp-(t48)TuIDRCD and mTuIDRCD

Similar to our previous work with the crystallization of MBP-cyanase (Schlachter et al., 2017), the MBP fragment was not present in the crystal structure of MBP-(t48)TuIDRCD. Therefore, the nomenclature mbp-(t48)TuIDRCD will be used to describe the fragment of the fusion construct MBP-(t48)TuIDRCD that was in the crystal structure. The mTuIDRCD construct was also crystallized. mbp-(t48)TuIDRCD and mTuIDRCD crystallized in a monoclinic system with four and two protein chains present in the asymmetric unit, respectively. In the mbp-(t48)TuIDRCD structure, each chain consists of residues 56–259 (with respect to the complete sequence reported in Uniprot (T1K8P1)) where the first eight amino acids (residues 48–55) of the truncated recombinant dioxygenase studied here are not visible in the electron density, nor is the TEV cut site and 6xHis-tag on the C-terminus. β-mercaptoethanol (β-ME) was used in purification buffers, but each chain starts at C56 which forms a disulfide bridge with C99 on the same chain. The structure of the mTuIDRCD is almost identical to the structure of mbp-(t48)TuIDRCD. In mTuIDRCD, the N-terminal residues 23–54 are disordered which is consistent with XtalPred predictions (Slabinski et al., 2007), and is the main reason these residues were excluded in the design of (t48)TuIDRCD, (t48)TuIDRCD-MBP, and MBP-(t48)TuIDRCD. The protein chains from both crystal structures superpose with RMSD values of ~0.6 Å over 198 aligned C_α atoms.

TuIDRCD contains eight β-strands that form a β-sandwich and two α-helices (Figs. 5 and 6). The β-sandwich core is conserved with most intradiol-ring cleavage dioxygenases (Bianchetti et al., 2013). The overall fold of dioxygenase is most similar to that of SACTE_2871 (PDB code: 4ILT; Fig. 5C) from *Streptomyces* sp. SirexAA-E which was used as

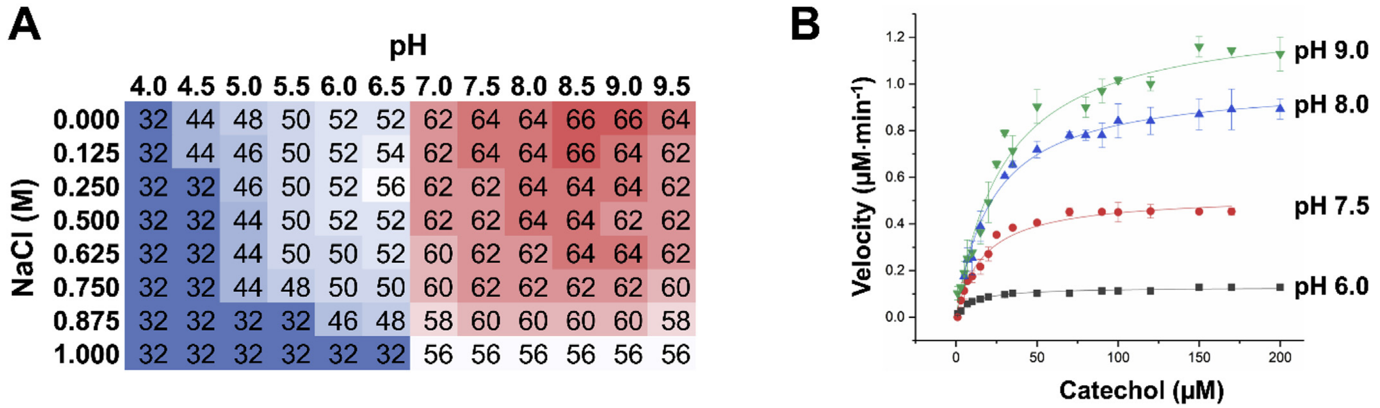

NaCl (M) \ pH	4.0	4.5	5.0	5.5	6.0	6.5	7.0	7.5	8.0	8.5	9.0	9.5
0.000	32	44	48	50	52	52	62	64	64	66	66	64
0.125	32	44	46	50	52	54	62	64	64	66	64	62
0.250	32	32	46	50	52	56	62	62	64	64	64	62
0.500	32	32	44	50	52	52	62	62	64	64	62	62
0.625	32	32	44	50	50	52	60	62	62	64	64	62
0.750	32	32	44	48	50	50	60	62	62	62	62	60
0.875	32	32	32	32	46	48	58	60	60	60	60	58
1.000	32	32	32	32	32	32	56	56	56	56	56	56

Fig. 4. *A*, Effect of pH and salt concentration on stability of mTuIDRCD. Blue displays low melting temperature, white is average, and red is high melting temperature. All temperatures are in °C. The standard deviation was typically less than 1 °C for all experiments. *B*, Michaelis-Menten graphs representing the initial velocity (μM min^{-1}) vs catechol concentration (μM) in pH 6.0. 7.5, 8.0 and 9.0. The absorbance of *cis,cis*-muconic acid was measured at 260 nm with the extinction coefficient of 16,800 M^{-1} cm^{-1} (Guzik et al., 2013c). (For interpretation of the references to color in this figure legend, the reader is referred to the Web version of this article.)

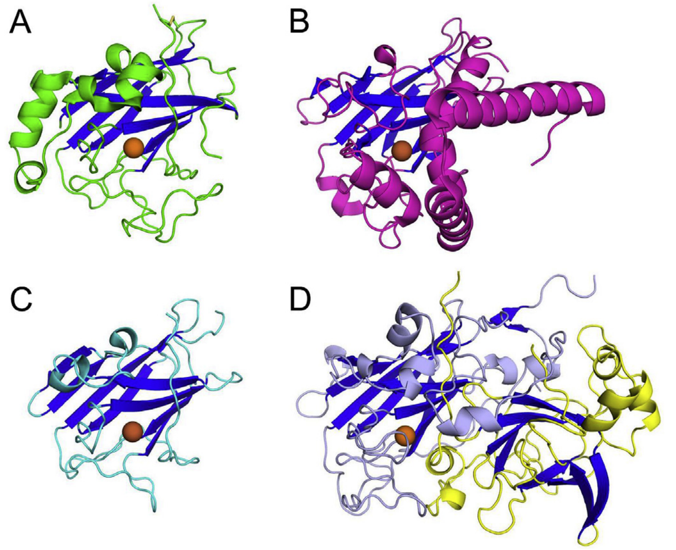

Fig. 5. *A*, Cartoon representation of mTuIDRCD (PDB code: 6BDJ). The β-sandwich core is conserved in ID-RCDs, and it was used to align in similar orientation all depicted structures. β-strands are marked in blue. *B*, Structure of a single chain of catechol 1,2-dioxygenase from *R. opacus* (PDB code: 3I51). *C*, SACTE_2871 - dioxygenase from *Streptomyces* sp. SirexAA-E (PDB code: 4ILV). *D*, Protocatechuate 3,4-dioxygenase from *P. putida* (α and β chains; PDB code: 4WHR). Position of the iron is marked with orange spheres. Only β chain binds Fe^{3+}. (For interpretation of the references to color in this figure legend, the reader is referred to the Web version of this article.)

the starting model for molecular replacement (Bianchetti et al., 2013). However, there is only a 17% sequence identity and 34% sequence similarity between TuIDRCD and SACTE_2871. Dali (Holm and Rosenstrom, 2010) was used to search for proteins similar to TuIDRCD and several dioxygenases were identified: catechol 1,2-dioxygenase from *Burkholderia multivorans* (PDB code 5UMH, 167/307 residues aligned, RMSD 2.4 Å, 26% sequence identity); 1,2-dioxygenase from *Burkholderia ambifaria* (PDB code: 5VXT, 166/311 residues aligned, RMSD 2.5 Å, 24% sequence identity); 3-chlorocatechol 1,2-dioxygenase from *Rhodococcus opacus 1Cp* (PDB code: 2BOY, 156/248 residues aligned, RMSD 2.0 Å, 24% sequence identity); hydroxyquinol 1,2-dioxygenase from *Pseudomonas putida* DLL-E4 (PDB code: 3N9T, 158/286 residues aligned, RMSD 2.4 Å, 23% sequence identity) and many other dioxygenases that do not have more than 25% of sequence identity to TuIDRCD over the aligned region.

TuIDRCD does not have an extensive N-terminal dimerization domain, an attribute common to ID-RCDs (Bianchetti et al., 2013). In the crystal structures, both mbp-(t48)TuIDRCD and mTuIDRCD appear to be monomeric (Figs. 5 and 6) which is consistent with size exclusion chromatography results (data not shown). The interface area between neighboring monomers is around 600 $Å^2$ or 360 $Å^2$, which is below the cutoff value (856 $Å^2$) proposed for discrimination between homodimeric and monomeric proteins (Ponstingl et al., 2000). The quaternary structure of TuIDRCD is similar to that of SACTE_2871 which is currently the only other ID-RCD that is monomeric and has a crystal structure determined. However, in the case of SACTE_2871, the dioxygenase domain is fused with a lignin binding domain (Bianchetti et al., 2013).

Fe^{3+} binding sites in both mbp-(t48)TuIDRCD and mTuIDRCD structures were validated by the CheckMyMetal server (Zheng et al., 2008, 2014). All Fe^{3+} cations were refined with full occupancy. The non-heme Fe^{3+} is coordinated by two tyrosines and two histidines in each active site: Y118, Y163, H169, H171 (Fig. 6B). The ferric center is coordinated in a trigonal bipyramidal manner with the four active site residues and a water molecule/hydroxyl group which is common to ID-RCDs (Guzik et al., 2013d). The mTuIDRCD was incubated with catechol prior to crystallization; despite the catechol not being present in the crystal structure, the side chain of Y163 is observed in two different orientations that correspond to iron-bound and "displaced" conformations. In the second conformation, the hydroxyl oxygen atom is displaced by 6.0 Å from the position that is observed in the iron-bound form. The presence of the second conformation permits iron

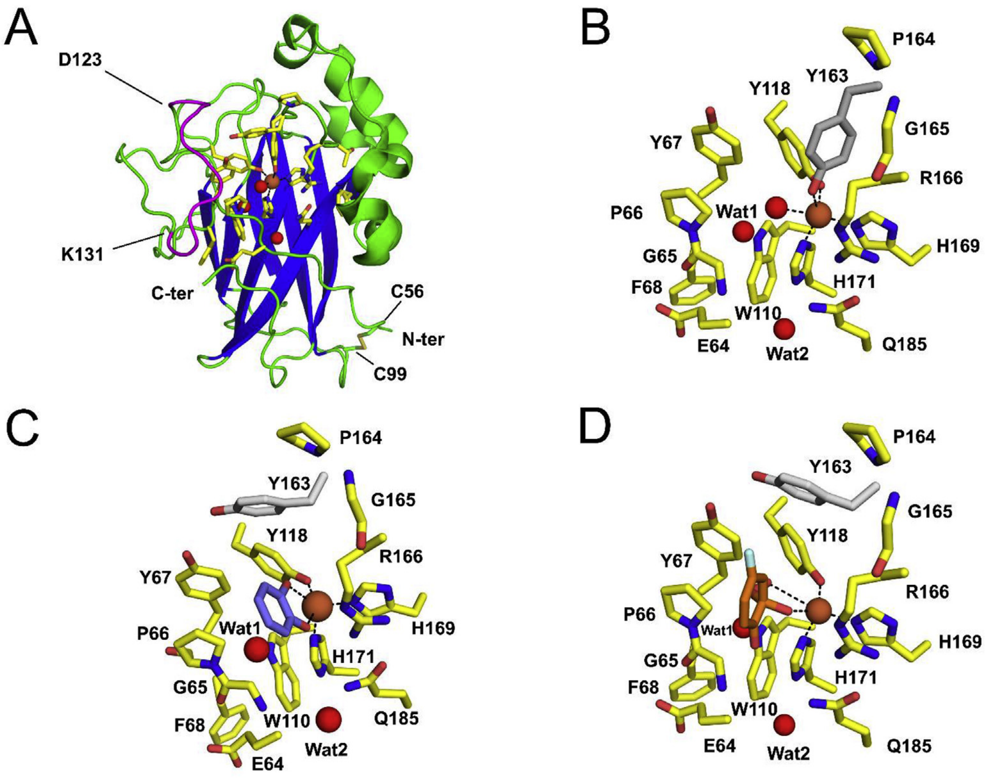

Fig. 6. *A*, An overall structure of mTuIDRCD. The core β-sandwich is marked in blue. The flexible D123-K131 region is shown in magenta. Residues near the active site that are conserved in both TuIDRCD and SACTE_2871 are shown as yellow sticks. Fe^{3+} is represented as an orange sphere, while water molecules are shown as red spheres. *B*, Active site of *apo*-mTuIDRCD. Residues coordinating the iron include H169, H171, Y118, and Y163. Y163 is shown in a conformation allowing for metal binding. Structurally conserved water molecules are labeled as Wat1 and Wat2. *C*, A putative *holo*-form of mTuIDRCD. Y163 is shown in a "displaced" conformation. Catechol molecule (purple sticks) is modeled based on the structure of catechol 1,2-dioxygenase from *R. opacus* 1CP (PDB code: 3HHY). *D*, A putative alkylperoxo reaction intermediate (orange sticks) modeled based on a structure of protocatechuate 3,4-dioxygenase from *P. putida* (PDB code: 4WHQ). (For interpretation of the references to color in this figure legend, the reader is referred to the Web version of this article.)

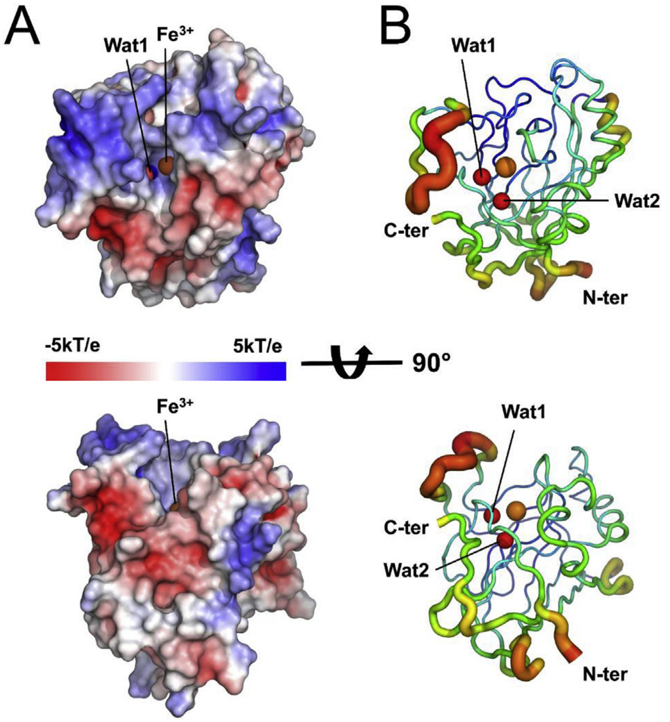

Fig. 7. *A*, Distribution of charges on a surface of TuIDRCD. A protein chain with Y163 facing away from Fe^{3+} was used to generate the molecular surface. *B*, Trace of the TuIDRCD main chain showing a relative mobility of various protein fragments. A diameter of the ribbon is proportional to B-factor value. Positively charged D123-K131 loop region found near the active site has a significant mobility. Structurally conserved water molecules are labeled as Wat1 and Wat2.

environment comparisons in *apo* and *holo*-forms of the enzyme (Fig. 6). Comparison of mTuIDRCD with the catechol bound structure of catechol 1,2-dioxygenase from *R. opacus* 1CP (PDB code: 3HHY) shows changes in the coordination of Fe^{3+} upon substrate binding (Fig. 6) (Matera et al., 2010).

Comparison of chains from TuIDRCD crystal structures reveals significant conformational flexibility of the D123-K131 region that is close to the metal binding site (Fig. 7). This region includes several basic residues that, in the crystal structure, have mostly disordered side chains. However, in two chains of the structure of mbp-(t48)TuIDRCD, the side chains of K128 point toward the metal binding site.

Analysis of TuIDRCD, SACTE_2871, catechol 1,2-dioxygenase from *Rhodococcus opacus* and other ID-RCDs revealed presence of two structurally conserved water molecules. One of them (Wat 1, Fig. 6B) forms H-bonds with the peptide backbone at E64 and Y67, and side chain of W110. In addition, in the *apo*-form of the enzyme, Water 1 forms a H-bond with the hydroxyl/water molecule coordinating iron. The second conserved water molecule (Wat 2; Fig. 6B) forms H-bonds with the peptide backbone of G63 and G184, as well as side chain Nδ1 of H171. Water 2 molecule is completely buried by residues.

4. Discussion

4.1. Origin of TuIDRCD

T. urticae is able to feed on more than 1100 plant species and therefore is considered to be one of the most polyphagous arthropod herbivores (Jeppson et al., 1975). This organism is not only able to detoxify various natural compounds originating from plants, but it also has an exceptional ability for developing pesticide resistance (Grbic et al., 2007; Van Leeuwen and Dermauw, 2016; Van Leeuwen et al., 2015). Some of the proteins, like ID-RCDs, used by *T. urticae* for xenobiotic detoxification were acquired by a lateral gene transfer. Phylogenetic analysis suggests that TuIDRCD was acquired by the spider mite from a fungal source (Fig. 2). The gene coding for TuIDRCD is the only in *T. urticae* that contains an intron (Dermauw et al., 2013). The TuIDRCD reported here (*Tetur07g02040*) is not only the first spider mite dioxygenase that has been characterized on the molecular level, but is also the first structurally characterized ID-RCD originating from a eukaryote. All previously structurally characterized ID-RCDs are of bacterial origin (Fig. 2) and the closest bacterial homolog (SACTE_2871; (Bianchetti et al., 2013)) with the structure determined has 17% sequence identity and 34% sequence similarity to TuIDRCD. Furthermore, TuIDRCD shares only 23–30% identity and 33–53% similarity with residues of other ID-RCDs identified in *T. urticae*.

4.2. Structure of TuIDRCD

TuIDRCD is not only very distinct from its bacterial homologs in terms of the source of origin and primary structure, but it also has quite unique structural features. The structures that we have determined (mbp-(t48)TuIDRCD and mTuIDRCD) clearly indicate that the N-terminal fragment of the protein is flexible which is in agreement with predictions made based on the protein sequence. The ordered and well-structured part of the protein starts from C56 which forms a disulfide bridge with C99. Comparison of sequences suggests that this disulfide bridge is most likely present in 14 out of the 17 ID-RCDs identified in the *T. urticae* genome; the exceptions are *Tetur01g00490, Tetur04g00150,* and *Tetur07g06560*. TuIDRCD has two additional cysteine residues in the flexible N-terminal part of the protein (C25 and C40), but these amino acids are not conserved among the *T. urticae* proteins. Interestingly, superposition of TuIDRCD and SACTE_2871 (PDB code: 4ILT) structures reveals that C99 from the spider mite protein corresponds to C119 from the *Streptomyces* protein. C119 of SACTE_2871 forms an interchain disulfide bridge with a symmetry related molecule. However, most likely formation of this intermolecular bridge is an effect of crystallization of a truncated version of the protein (residues 77–230). This is consistent with the fact that in another crystal structure of SACTE_2871 (PDB code: 4ILV) such an intermolecular disulfide linkage is not present (Bianchetti et al., 2013). Therefore, it is very likely that the TuIDRCD disulfide bridge formed by C56 and C99 is homologous to C72 and C119 in SACTE_2871.

Another characteristic structural feature of TuIDRCD is its quaternary structure. This protein, similar to SACTE_2871, is monomeric and lacks the N-terminal oligomerization domain, while other proteins from this family are homodimeric or heterooligomeric. Furthermore, SACTE_2871 has a C-terminal domain that is involved in lignin binding (Bianchetti et al., 2013). The function of the N-terminal (residues 23–55) of TuIDRCD is not known, but despite being disordered, it clearly stabilizes the protein compared to (t48)TuIDRCD, which was very unstable during expression and purification (data not shown). It is possible that this fragment of enzyme is involved in interactions with other proteins or molecules similarly to the function of C-terminal domain of SACTE_2871 (Bianchetti et al., 2013).

The TuIDRCD iron binding site is composed of the same amino acids as in bacterial homologs, also reflected in very similar optical and EPR spectroscopic properties. There are two histidine (H169 and H171) and two tyrosine residues (Y118 and Y163) that coordinate Fe^{3+}. Similarly, as in other ID-RCDs, Y163 is coordinating the metal in the resting state of the enzyme (Figs. 1 and 6) but is very likely displaced upon substrate binding; Y163 also “swings” back and binds to the metal in the later steps of the reaction (Borowski and Siegbahn, 2006b; Knoot et al., 2015; Valley et al., 2005). Structural comparison of TuIDRCD with other catechol 1,2-dioxygenases shows that residues P66, W110, R166 and Q185 are completely conserved. R166 and Q185 sidechains form H-bonds, and R166 may be responsible for stabilization of reaction intermediates (Borowski and Siegbahn, 2006b). Analysis of TuIDRCD crystal structures revealed two water molecules in the vicinity of the Fe^{3+} binding site that most likely have a structural function (Fig. 6).

4.3. Enzymatic activity

The mTuIDRCD is able to cleave catechol, which results in the formation of *cis, cis*-muconic acid (Fig. 1); however, under the same conditions the enzyme is not able to use 3,4-dihydroxybenzoate as a substrate (data not shown). Based on kinetic data, the enzyme is more efficient in solutions with basic pH. K_M values observed for catechol are in a low-micromolar range and are similar to those observed for various bacterial homologs. However, k_{cat} and k_{cat}/K_M values indicate that TuIDRCD is more than 2-fold less efficient in cleaving the substrate in comparison with SACTER_2871 and 2–4 fold less efficient in comparison with some bacterial 1,2-dioxygenases (Ferraroni et al., 2006, 2013; Matera et al., 2010; Micalella et al., 2011). The lack of the efficiency may be related to the fact that catechol is not amongst the normal panel of catecholic substrates for the enzyme, or that TuIDRCD requires an activator/regulatory molecule (or molecules) in order to have full enzymatic potential. Evidence may be provided by the failure of the 4-methylcatechol substrate to elicit perturbations to the optical spectrum of TuIDRCD that occur upon ligation of the substrate. It is also notable that protocatechuate 3,4-dioxygenases form heterooligomers (Fig. 5D). The heterooligomers are composed from α and β units, and both units participate in formation of the active site, although only the β unit provides Fe^{3+} binding residues (Frazee et al., 1993; Guzik et al., 2013d). Interestingly, we did not observe cleavage of protocatechuate by mTuIDRCD, while the enzyme preferred 4-methylcatechol over catechol as the substrate. It clearly shows that the type of the catechol substituent is important in gating binding and catalysis by TuIDRCD. The reason why TuIDRCD is catalytically notably less efficient than bacterial ID-RCDs is not clear, yet the observed variance of its activity for substrates with various 4-substituents allows us to speculate that at least one of the elementary steps, whose reaction energy affects the overall barrier, is the culprit. It might be either the O_2 binding step, or the following step whereby the peroxo intermediate changes its conformation (Fig. 1). In the former case the substituent effect would be electronic in nature, i.e. electron withdrawing groups deplete π electron density of the ring and hence deactivate it, whereas in the latter the effect would be steric in nature, i.e. non-bonded interactions between the substituent and protein residues lining the active site pocket would tune the energy difference between the two conformers of the peroxo intermediate. It is also worth mentioning that the active site in TuIDRCD is significantly more open in comparison with bacterial homologs that have their structures determined.

The existence of the proliferated family of ID-RCD enzymes in *T. urticae* can be linked to its ability to feed on an extremely wide range of host plants. Currently, the natural substrates for *tetur07g02040* (TuIDRCD) are not known. However, the presence of a highly homologous enzyme in *T. evansi* (Uniprot id: K9UU26), an oligophagous mite species that feeds on solanaceous plants, suggests that either *tetur07g02040* processes substrates conserved between mite species, or that *tetur07g02040* evolved the ability to process a greater spectrum of substrates. Similarly, proteins homologous to *tetur07g02040* were also identified in *Panonychus citri* (citrus red mite) and *Panonychus ulmi* (European red mite) (Bajda et al., 2015). Therefore, comparative analysis of TuIDRCD, TeIDRCD as well as *P. citri* and *P. ulmi* dioxygenases activities against a panel of potential substrates may allow discrimination between these possibilities. Furthermore, if TuIDRCD is involved in detoxification, then it is expected that it will be secreted and active in the digestive tract, a compartment where plant and mite compartments intercept. At present, it is not known where within the gut digestion and detoxification occur (Bensoussan et al., 2018). However, the basic range of optimal pH for the TuIDRCD activity suggests that its activity may not coincide with the activities of digestive proteinases, as their optimal range is within the acidic pH (Santamaria et al., 2015).

Accession numbers

Coordinates and structure factors have been deposited to the PDB with accession codes 5VG2 (mbp-(t48)TuIDRCD) and 6BDJ (mTuIDRCD).

Conflicts of interest

The authors declare that they have no conflicts of interest with the contents of this article.

Author contributions

M.C., M.G., V.G. and T.V.L. initiated the studies. C.R.S performed cloning. C.R.S., L.D. and V.K. produced, and crystallized proteins. C.R.S and L.D. performed structural analysis. C.R.S and L.D. performed enzymatic studies and DSF experiments. J.A. and T.M.M. performed and analyzed EPR experiments. N.W. and T.V.L. conducted phylogenetic analysis. T.B. performed analysis of the enzyme activity. All authors participated in the analysis of data and contributed to writing the manuscript with a final review by M.C.

Acknowledgments

We would like to thank Dr. Lijiang He (Mass Spectrometry Manager, University of South Carolina) for performing ICP-MS experiments. We also would like to thank Dr. Caryn Outten for access to the microplate reader.

Structural results shown in this report are derived from data collected at Southeast Regional Collaborative Access Team (SER-CAT; 22 ID) beamline at the Advanced Photon Source, Argonne National Laboratory. Supporting institutions may be found at www.ser-cat.org/members.html. Use of the Advanced Photon Source was supported by the U.S. Department of Energy, Office of Science, Office of Basic Energy Sciences, under Contract Nos. DE-AC02-06CH11357 and W-31-109-Eng-38. This work was partially supported by an ASPIRE II and ASPIRE III grants from the Office of the Vice President of Research at the University of South Carolina. C.R.S. and M.C. were partially supported by R01AI077653 grant from National Institute of Allergy and Infectious Diseases. The content is solely the responsibility of the authors and does not necessarily represent the official views of the National Institutes of Health. M.G. and V.G. acknowledge funding by the Government of Canada through Genome Canada and the Ontario Genomics Institute (OGI-046) and Ontario Research Fund – Research Excellence Round 8 (RE08-067). N.W. was supported by a Marie Sklodowska-Curie Action (MSCA) Individual fellowship (658795-DOGMITE) of Horizon 2020 and a Flanders Research Foundation (FWO) fellowship (12T9818N). T.V.L. was supported by the Fund for Scientific Research Flanders (FWO) (Grant Nos. G009312Nand G053815N). T.V.L., V.G. and M.G. were supported by the European Commission (EC contract 618105) via FACCE ERA-NET Plus and FACCE-JP (Genomite, project ID 137). TVL has received funding from the European Research Council (ERC) under the European Union's Horizon 2020 research and innovation programme (grant agreement n° 772026).

Appendix A. Supplementary data

Supplementary data to this article can be found online at https://doi.org/10.1016/j.ibmb.2018.12.001.

References

Bajda, S., Dermauw, W., Greenhalgh, R., Nauen, R., Tirry, L., Clark, R.M., Van Leeuwen, T., 2015. Transcriptome profiling of a spirodiclofen susceptible and resistant strain of the European red mite Panonychus ulmi using strand-specific RNA-seq. BMC Genomics 16, 974.

Becker, J.S., Zoriy, M., Matusch, A., Wu, B., Salber, D., Palm, C., Becker, J.S., 2010. Bioimaging of metals by laser ablation inductively coupled plasma mass spectrometry (LA-ICP-MS). Mass Spectrom. Rev. 29, 156–175.

Bensoussan, N., Zhurov, V., Yamakawa, S., O'Neil, C.H., Suzuki, T., Grbic, M., Grbic, V., 2018. The digestive system of the two-spotted spider mite, Tetranychus urticae (Koch), in the context of the mite-plant interaction. Front. Plant Sci. 9, 1206. https://doi.org/10.3389/fpls.2018.01206.

Berman, H.M., Westbrook, J., Feng, Z., Gilliland, G., Bhat, T.N., Weissig, H., Shindyalov, I.N., Bourne, P.E., 2000. The protein Data Bank. Nucleic Acids Res. 28, 235–242.

Bianchetti, C.M., Harmann, C.H., Takasuka, T.E., Hura, G.L., Dyer, K., Fox, B.G., 2013. Fusion of dioxygenase and lignin-binding domains in a novel secreted enzyme from cellulolytic Streptomyces sp. SirexAA-E. J. Biol. Chem. 288, 18574–18587.

Booth, W.T., Schlachter, C.R., Pote, S., Ussin, N., Mank, N.J., Klapper, V., Offermann, L.R., Tang, C., Hurlburt, B.K., Chruszcz, M., 2018. Impact of an N-terminal polyhistidine tag on protein thermal stability. ACS Omega 3, 760–768.

Borowski, T., Siegbahn, P.E., 2006a. Mechanism for catechol ring cleavage by non-heme iron intradiol dioxygenases: a hybrid DFT study. J. Am. Chem. Soc. 128, 12941–12953.

Borowski, T., Siegbahn, P.E.M., 2006b. Mechanism for catechol ring cleavage by non-heme iron intradiol dioxygenases: a hybrid DFT study. J. Am. Chem. Soc. 128, 12941–12953.

Broderick, J.B., 1999. Catechol dioxygenases. Essays Biochem. 34, 173–189.

Brown, C.K., Vetting, M.W., Earhart, C.A., Ohlendorf, D.H., 2004. Biophysical analyses of designed and selected mutants of protocatechuate 3,4-dioxygenase1. Annu. Rev. Microbiol. 58, 555–585.

Bugg, T.D.H., 2003. Dioxygenase enzymes: catalytic mechanisms and chemical models. Tetrahedron 59, 7075–7101.

Caglio, R., Valetti, F., Caposio, P., Gribaudo, G., Pessione, E., Giunta, C., 2009. Fine-tuning of catalytic properties of catechol 1,2-dioxygenase by active site tailoring. Chembiochem 10, 1015–1024.

Caglio, R., Pessione, E., Valetti, F., Giunta, C., Ghibaudi, E., 2013. An EPR, thermostability and pH-dependence study of wild-type and mutant forms of catechol 1,2-dioxygenase from Acinetobacter radioresistens S13. Biometals 26, 75–84.

Chen, W., Hasegawa, D.K., Kaur, N., Kliot, A., Pinheiro, P.V., Luan, J., Stensmyr, M.C., Zheng, Y., Liu, W., Sun, H., 2016. The draft genome of whitefly Bemisia tabaci MEAM1, a global crop pest, provides novel insights into virus transmission, host adaptation, and insecticide resistance. BMC Biol. 14, 110.

Cowtan, K., 2006. The Buccaneer software for automated model building. 1. Tracing protein chains. Acta Crystallogr. 62, 1002–1011.

Darriba, D., Taboada, G.L., Doallo, R., Posada, D., 2011. ProtTest 3: fast selection of best-fit models of protein evolution. Bioinformatics 27, 1164–1165.

Davis, M.I., Orville, A.M., Neese, F., Zaleski, J.M., Lipscomb, J.D., Solomon, E.I., 2002. Spectroscopic and electronic structure studies of protocatechuate 3, 4-dioxygenase: nature of Tyrosinate− Fe (III) bonds and their contribution to reactivity. J. Am. Chem. Soc. 124, 602–614.

Davis, I.W., Leaver-Fay, A., Chen, V.B., Block, J.N., Kapral, G.J., Wang, X., Murray, L.W., Arendall 3rd, W.B., Snoeyink, J., Richardson, J.S., Richardson, D.C., 2007. MolProbity: all-atom contacts and structure validation for proteins and nucleic acids. Nucleic Acids Res. 35, W375–W383.

DeLano, W.,S., 2002. The PyMOL Molecular Graphics System.

Dermauw, W., Wybouw, N., Rombauts, S., Menten, B., Vontas, J., Grbic, M., Clark, R.M., Feyereisen, R., Van Leeuwen, T., 2013. A link between host plant adaptation and pesticide resistance in the polyphagous spider mite Tetranychus urticae. In: Proceedings of the National Academy of Sciences of the United States of America.

Emsley, P., Cowtan, K., 2004. Coot: model-building tools for molecular graphics. Acta Crystallogr. 60, 2126–2132.

Eschenfeldt, W.H., Makowska-Grzyska, M., Stols, L., Donnelly, M.I., Jedrzejczak, R., Joachimiak, A., 2013. New LIC vectors for production of proteins from genes containing rare codons. J. Struct. Funct. Genom. 14, 135–144.

Faddeeva-Vakhrusheva, A., Derks, M.F., Anvar, S.Y., Agamennone, V., Suring, W., Smit, S., van Straalen, N.M., Roelofs, D., 2016. Gene family evolution reflects adaptation to soil environmental stressors in the genome of the collembolan Orchesella cincta. Genome Biol. Evol. 8, 2106–2117.

Ferraroni, M., Kolomytseva, M.P., Solyanikova, I.P., Scozzafava, A., Golovleva, L.A., Briganti, F., 2006. Crystal structure of 3-chlorocatechol 1,2-dioxygenase key enzyme of a new modified ortho-pathway from the Gram-positive Rhodococcus opacus 1CP grown on 2-chlorophenol. J. Mol. Biol. 360, 788–799.

Ferraroni, M., Kolomytseva, M., Scozzafava, A., Golovleva, L., Briganti, F., 2013. X-ray structures of 4-chlorocatechol 1,2-dioxygenase adducts with substituted catechols: new perspectives in the molecular basis of intradiol ring cleaving dioxygenases specificity. J. Struct. Biol. 181, 274–282.

Frazee, R.W., Livingston, D.M., LaPorte, D.C., Lipscomb, J.D., 1993. Cloning, sequencing, and expression of the Pseudomonas putida protocatechuate 3,4-dioxygenase genes. J. Bacteriol. 175, 6194–6202.

Gasteiger, E., Gattiker, A., Hoogland, C., Ivanyi, I., Appel, R.D., Bairoch, A., 2003. ExPASy: the proteomics server for in-depth protein knowledge and analysis. Nucleic Acids Res. 31, 3784–3788.

Grbic, M., Khila, A., Lee, K.Z., Bjelica, A., Grbic, V., Whistlecraft, J., Verdon, L., Navajas, M., Nagy, L., 2007. Mity model: Tetranychus urticae, a candidate for chelicerate model organism. Bioessays 29, 489–496.

Grbic, M., Van Leeuwen, T., Clark, R.M., Rombauts, S., Rouze, P., Grbic, V., Osborne, E.J., Dermauw, W., Ngoc, P.C., Ortego, F., Hernandez-Crespo, P., Diaz, I., Martinez, M., Navajas, M., Sucena, E., Magalhaes, S., Nagy, L., Pace, R.M., Djuranovic, S., Smagghe, G., Iga, M., Christiaens, O., Veenstra, J.A., Ewer, J., Villalobos, R.M., Hutter, J.L., Hudson, S.D., Velez, M., Yi, S.V., Zeng, J., Pires-daSilva, A., Roch, F., Cazaux, M., Navarro, M., Zhurov, V., Acevedo, G., Bjelica, A., Fawcett, J.A., Bonnet, E., Martens, C., Baele, G., Wissler, L., Sanchez-Rodriguez, A., Tirry, L., Blais, C., Demeestere, K., Henz, S.R., Gregory, T.R., Mathieu, J., Verdon, L., Farinelli, L., Schmutz, J., Lindquist, E., Feyereisen, R., Van de Peer, Y., 2011. The genome of Tetranychus urticae reveals herbivorous pest adaptations. Nature 479, 487–492.

Guzik, U., Hupert-Kocurek, K., Salek, K., Wojcieszynska, D., 2013a. Influence of metal ions on bioremediation activity of protocatechuate 3,4-dioxygenase from Stenotrophomonas maltophilia KB2. World J. Microbiol. Biotechnol. 29, 267–273.

Guzik, U., Hupert-Kocurek, K., Sitnik, M., Wojcieszynska, D., 2013b. High activity catechol 1,2-dioxygenase from Stenotrophomonas maltophilia strain KB2 as a useful tool in cis,cis-muconic acid production. Antonie Van Leeuwenhoek 103, 1297–1307.

Guzik, U., Hupert-Kocurek, K., Sitnik, M., Wojcieszyńska, D., 2013c. High activity catechol 1, 2-dioxygenase from Stenotrophomonas maltophilia strain KB2 as a useful tool in cis, cis-muconic acid production. Antonie van Leeuwenhoek 103, 1297–1307.

Guzik, U., Hupert-Kocurek, K., Wojcieszyńska, D., 2013d. Intradiol Dioxygenases—the Key Enzymes in Xenobiotics Degradation, Biodegradation of Hazardous and Special Products. InTech.

Holm, L., Rosenstrom, P., 2010. Dali server: conservation mapping in 3D. Nucleic Acids Res. 38, W545–W549.

Jeppson, L.R., Keifer, H.H., Baker, E.W., 1975. Mites Injurious to Economic Plants. Univ of California Press.

Jurrus, E., Engel, D., Star, K., Monson, K., Brandi, J., Felberg, L.E., Brookes, D.H., Wilson, L., Chen, J., Liles, K., Chun, M., Li, P., Gohara, D.W., Dolinsky, T., Konecny, R., Koes, D.R., Nielsen, J.E., Head-Gordon, T., Geng, W., Krasny, R., Wei, G.W., Holst, M.J., McCammon, J.A., Baker, N.A., 2018. Improvements to the APBS biomolecular solvation software suite. Protein Sci. 27, 112–128.

Knoot, C.J., Purpero, V.M., Lipscomb, J.D., 2015. Crystal structures of alkylperoxo and anhydride intermediates in an intradiol ring-cleaving dioxygenase. Proc. Natl. Acad. Sci. U.S.A. 112, 388–393.

Krissinel, E., Henrick, K., 2004. Secondary-structure matching (SSM), a new tool for fast protein structure alignment in three dimensions. Acta Crystallogr. 60, 2256–2268.

Krissinel, E., Henrick, K., 2007. Inference of macromolecular assemblies from crystalline state. J. Mol. Biol. 372, 774–797.

Laskowski, R.A., 2017. The ProFunc function prediction server. Methods Mol. Biol. 1611, 75–95.

Matera, I., Ferraroni, M., Kolomytseva, M., Golovleva, L., Scozzafava, A., Briganti, F., 2010. Catechol 1,2-dioxygenase from the Gram-positive Rhodococcus opacus 1CP: quantitative structure/activity relationship and the crystal structures of native enzyme and catechols adducts. J. Struct. Biol. 170, 548–564.

Micalella, C., Martignon, S., Bruno, S., Pioselli, B., Caglio, R., Valetti, F., Pessione, E., Giunta, C., Rizzi, M., 2011. X-ray crystallography, mass spectrometry and single crystal microspectrophotometry: a multidisciplinary characterization of catechol 1,2 dioxygenase. Biochim. Biophys. Acta 1814, 817–823.

Minor, W., Cymborowski, M., Otwinowski, Z., Chruszcz, M., 2006. HKL-3000: the integration of data reduction and structure solution–from diffraction images to an initial model in minutes. Acta Crystallogr. 62, 859–866.

Murshudov, G.N., Skubak, P., Lebedev, A.A., Pannu, N.S., Steiner, R.A., Nicholls, R.A., Winn, M.D., Long, F., Vagin, A.A., 2011. REFMAC5 for the refinement of macromolecular crystal structures. Acta Crystallogr. Sect. D Biol. Crystallogr. 67, 355–367.

Orville, A.M., Lipscomb, J.D., 1993. Simultaneous binding of nitric oxide and isotopically labeled substrates or inhibitors by reduced protocatechuate 3,4-dioxygenase. J. Biol. Chem. 268, 8596–8607.

Otwinowski, Z., Minor, W., 1997. Processing of X-ray diffraction data collected in oscillation mode. In: Methods in Enzymology: Macromolecular Crystallography , Part A. Academic Press, New York, pp. 307–326.

Painter, J., Merritt, E.A., 2006. TLSMD web server for the generation of multi-group TLS models. J. Appl. Crystallogr. 39, 109–111.

Pettersen, E.F., Goddard, T.D., Huang, C.C., Couch, G.S., Greenblatt, D.M., Meng, E.C., Ferrin, T.E., 2004. UCSF Chimera–a visualization system for exploratory research and analysis. J. Comput. Chem. 25, 1605–1612.

Ponstingl, H., Henrick, K., Thornton, J.M., 2000. Discriminating between homodimeric and monomeric proteins in the crystalline state. Proteins 41, 47–57.

Ronquist, F., Teslenko, M., Van Der Mark, P., Ayres, D.L., Darling, A., Höhna, S., Larget, B., Liu, L., Suchard, M.A., Huelsenbeck, J.P., 2012. MrBayes 3.2: efficient Bayesian phylogenetic inference and model choice across a large model space. Syst. Biol. 61, 539–542.

Sainsbury, P.D., Mineyeva, Y., Mycroft, Z., Bugg, T.D., 2015. Chemical intervention in bacterial lignin degradation pathways: development of selective inhibitors for intradiol and extradiol catechol dioxygenases. Bioorg. Chem. 60, 102–109.

Santamaria, M.E., Gonzalez-Cabrera, J., Martinez, M., Grbic, V., Castanera, P., Diaz, L., Ortego, F., 2015. Digestive proteases in bodies and faeces of the two-spotted spider mite, Tetranychus urticae. J. Insect Physiol. 78, 69–77.

Schlachter, C.R., Klapper, V., Wybouw, N., Radford, T., Van Leeuwen, T., Grbic, M., Chruszcz, M., 2017. Structural characterization of a eukaryotic cyanase from Tetranychus urticae. J. Agric. Food Chem. 65, 5453–5462.

Slabinski, L., Jaroszewski, L., Rychlewski, L., Wilson, I.A., Lesley, S.A., Godzik, A., 2007. XtalPred: a web server for prediction of protein crystallizability. Bioinformatics 23, 3403–3405.

Tchesnokov, E.P., Wilbanks, S.M., Jameson, G.N., 2012. A strongly bound high-spin iron (II) coordinates cysteine and homocysteine in cysteine dioxygenase. Biochemistry 51, 257–264.

Travkin, V.M., Jadan, A.P., Briganti, F., Scozzafava, A., Golovleva, L.A., 1997. Characterization of an intradiol dioxygenase involved in the biodegradation of the chlorophenoxy herbicides 2,4-D and 2,4,5-T. FEBS Lett. 407, 69–72.

Tsai, S.C., Li, Y.K., 2007. Purification and characterization of a catechol 1,2-dioxygenase from a phenol degrading Candida albicans TL3. Arch. Microbiol. 187, 199–206.

UniProt, C., 2015. UniProt: a hub for protein information. Nucleic Acids Res. 43, D204–D212.

Vagin, A., Teplyakov, A., 1997. MOLREP: an automated program for molecular replacement. J. Appl. Crystallogr. 30, 1022–1025.

Vaillancourt, F.H., Bolin, J.T., Eltis, L.D., 2006. The ins and outs of ring-cleaving dioxygenases. Crit. Rev. Biochem. Mol. Biol. 41, 241–267.

Valley, M.P., Brown, C.K., Burk, D.L., Vetting, M.W., Ohlendorf, D.H., Lipscomb, J.D., 2005. Roles of the equatorial tyrosyl iron ligand of protocatechuate 3,4-dioxygenase in catalysis. Biochemistry 44, 11024–11039.

Van Leeuwen, T., Dermauw, W., 2016. The molecular evolution of xenobiotic metabolism and resistance in chelicerate mites. Annu. Rev. Entomol. 61, 475–498.

Van Leeuwen, T., Tirry, L., Yamamoto, A., Nauen, R., Dermauw, W., 2015. The economic importance of acaricides in the control of phytophagous mites and an update on recent acaricide mode of action research. Pestic. Biochem. Physiol. 121, 12–21.

Weng, J.K., 2014. The evolutionary paths towards complexity: a metabolic perspective. New Phytol. 201, 1141–1149.

Widhalm, J.R., Dudareva, N., 2015. A familiar ring to it: biosynthesis of plant benzoic acids. Mol. Plant 8, 83–97.

Wojcik, A., Borowski, T., Broclawik, E., 2011. The mechanism of the reaction of intradiol dioxygenase with hydroperoxy probe A DFT study. Catal. Today 169, 207–216.

Yoshida, Y., Koutsovoulos, G., Laetsch, D.R., Stevens, L., Kumar, S., Horikawa, D.D., Ishino, K., Komine, S., Kunieda, T., Tomita, M., 2017. Comparative genomics of the tardigrades Hypsibius dujardini and Ramazzottius varieornatus. PLoS Biol. 15, e2002266.

Zheng, H., Chruszcz, M., Lasota, P., Lebioda, L., Minor, W., 2008. Data mining of metal ion environments present in protein structures. J. Inorg. Biochem. 102, 1765–1776.

Zheng, H., Chordia, M.D., Cooper, D.R., Chruszcz, M., Muller, P., Sheldrick, G.M., Minor, W., 2014. Validation of metal-binding sites in macromolecular structures with the CheckMyMetal web server. Nat. Protoc. 9, 156–170.